Progress in Oceanography 193 (2021) 102543

Contents lists available at ScienceDirect

Progress in Oceanography

journal homepage: www.elsevier.com/locate/pocean

Influence of multi-scale dynamics on the vertical nitrate distribution around the Kuroshio Extension: An investigation based on BGC-Argo and satellite data

Tao Wang [a], Fei Chai [b,c,*], Xiaogang Xing [b], Jue Ning [d], Wensheng Jiang [a], Stephen C. Riser [e]

[a] Key Laboratory of Marine Environment and Ecology, Ocean University of China, Qingdao, China
[b] State Key Laboratory of Satellite Ocean Environment Dynamics, Second Institute of Oceanography, Ministry of Natural Resources, Hangzhou, China
[c] School of Marine Sciences, University of Maine, Orono, ME, USA
[d] College of Oceanography, Hohai University, Nanjing, China
[e] School of Oceanography, University of Washington, Seattle, USA

ARTICLE INFO

Keywords:
Biogeochemical-Argo (BGC-Argo)
Nitrate
Satellite observation
Submesoscale
Kuroshio Extension (KE)

ABSTRACT

The vertical delivery of nutrients from deep water into the euphotic zone is one of the major limitations for the ocean primary productivity. In this study, the influence of multi-scale dynamics on the nitrate distribution observed by two BGC-Argo floats around the Kuroshio Extension is investigated. Vertical fluctuations of iso-nitrate surfaces and isopycnals were found to be correlated to the variation of absolute dynamic topography. In the subtropical Northwestern Pacific Ocean, subsurface nitrate concentration was found to be elevated inside a cyclonic mesoscale eddy during summer, while little nitrate was supplied into the surface layer, which was possibly due to the inhibition of seasonal thermocline. On the northern edge of the Kuroshio Extension, elevated euphotic-layer nitrate and surface chlorophyll concentrations were observed along the periphery of an anti-cyclonic eddy. In addition to horizontal advection, upwelling induced by the submesoscale dynamics is suggested to likely play an important role in the enhancements of nitrate and chlorophyll concentrations. The enhanced vertical delivery of nutrients from depth due to submesoscale dynamics has been hypothesized as a significant source for some satellite-observed events of high surface chlorophyll concentration, but direct evidence from in-situ observations is lacking. In this study, the synchronous occurrence of elevated nitrate and chlorophyll concentrations along the periphery of an anti-cyclonic eddy provides an evidence to support this hypothesis to some extent.

1. Introduction

In many regions of the world oceans, the insufficient supply of nutrients from depth into the euphotic zone (about 100 m near the surface) is a major limitation on ocean primary productivity (Mahadevan, 2016). The vertical delivery of nutrients may be induced by multi-scale dynamics, including large-scale Ekman pumping, mesoscale eddy pumping, internal waves, submesoscale secondary circulations, and turbulent mixing (Klein & Lapeyre, 2009; Gaube et al., 2013; Li & He, 2014; McGillicuddy, 2016; Ning et al., 2021). Thus, studying how these multi-scale dynamics influence the vertical distribution of nutrients is important for understanding the physical-biological interactions.

Influences of large-scale circulations and mesoscale eddies on the distribution of nutrients have been studied for several decades (e.g., Jenkins, 1988; Chelton et al., 2011). At the large scale, nitrate concentrations in the euphotic layer are generally low inside subtropical gyres due to the downward Ekman pumping, while they are higher inside subpolar gyres (Omand & Mahadevan, 2013; Xiu & Chai, 2020). Mesoscale eddies and internal waves could cause *iso*-surfaces of nutrients to heave vertically, thus potentially inducing mesoscale variability of the nutrient and chlorophyll concentrations in the euphotic layer (While & Haines, 2010). In recent years, oceanic submesoscale currents, which occur on a horizontal scale of 1–10 km and temporal scales of a few days, have been proposed to emerge as important structuring regimes for nutrients and chlorophyll. Horizontal advection and stirring have great effects on the elevated chlorophyll concentrations along the

* Corresponding author at: State Key Laboratory of Satellite Ocean Environment Dynamics, Second Institute of Oceanography, Ministry of Natural Resources, Hangzhou, China.
E-mail address: fchai@sio.org.cn (F. Chai).

https://doi.org/10.1016/j.pocean.2021.102543
Received 11 September 2020; Received in revised form 26 February 2021; Accepted 1 March 2021
Available online 6 March 2021

ocean fronts and filaments, as revealed in discrete snapshots of satellite views (Mahadevan, 2016; Lehahn et al., 2018; Xu et al., 2019). In addition to the horizontal advection, another relevant submesoscale mechanism proposed by previous studies is that ageostrophic secondary circulations upwell nutrients into the euphotic layer to support elevated chlorophyll concentration along fronts and filaments (Klein & Lapeyre, 2009; Mahadevan, 2016). Therefore, both horizontal and vertical motions are intrinsically linked in terms of how the submesoscale dynamics influence the distribution of chlorophyll concentrations. Fronts and filaments could be induced by several physical mechanisms (e.g., McWilliams, 2015; Barkan et al., 2019; Wang et al., 2021), and the geostrophic strain is one that usually occurs in regions with strong currents, such as the Kuroshio Extension (KE), Gulf Stream, and the periphery of mesoscale eddies (e.g., Gula et al., 2014; Barkan et al., 2017). Strain tends to compress fluid in one direction and stretch it in the perpendicular direction. When the principle axis of strain rate is perpendicular to the direction of horizontal density gradient, it tends to induce fronts or filaments (Gula et al., 2014; Wang et al., 2021). Once fronts or filaments are generated, ageostrophic secondary circulations are often induced in the cross-frontal direction (Capet et al., 2008) and this is proposed to be an important mechanism to transport nutrients into the euphotic layer (Mahadevan, 2016). Although vertical nutrients supply has been hypothesized to be one of the primary mechanisms for some observed events of high surface chlorophyll (CHL) concentrations along submesoscale fronts and filaments in the open ocean (e.g., Kahru et al., 2007; Brannigan, 2016; Liu & Levine, 2016; Zhang et al., 2019) and has been studied with numerical models (e.g., Calil & Richards, 2010; Lévy et al., 2012), there is little in-situ observed evidence from the nutrients profiles (Zhou et al., 2013; Hosegood et al., 2017; Naigai & Clayton, 2017).

As one of the most important sink for anthropogenic CO_2, the Kuroshio Extension (KE) plays an important role in the climate system (Cronin et al., 2008). Thus it is necessary to interpret the bio-chemical processes in terms of CO_2 uptake by the KE regions. The KE is a deep and large-scale front populated with mesoscale eddies, submesoscale fronts and filaments (Fassbender et al., 2017; Qiu et al., 2017; Xu et al., 2017; Luo et al., 2020). Thus, the bio-chemical processes in this region are influenced by multi-scale physical dynamics. To understand the physical-biological interactions around the KE region, it is necessary to study how the horizontal and vertical transports of nutrients are influenced by the multi-scale dynamics. At the large scale, the Kuroshio acts as a basin-scale subsurface nutrients conduit that transports large amounts of nutrients from the tropical ocean to the KE (Guo et al., 2013, Long et al., 2018; Guo et al., 2019; Naigai et al., 2019). In the KE region, to support the chlorophyll, sufficient supply of nutrients from subsurface into the euphotic zone is needed. Naigai and Clayton (2017) observed elevated nitrate concentration in a warm streamer on the north side of the KE, and they speculated that the vertical motions in the warm streamers were one of the final supply routes to the surface for nutrients transported by the Kuroshio. A recent numerical study showed that ageostrophic secondary circulations were formed around a warm mesoscale eddy on the northern edge of the KE (Luo et al., 2020). However, how the warm mesoscale eddies and their associated fronts influence the transport of nutrients is still not well-understood owing to insufficient observations in the KE region.

In recent years, Biogeochemical-Argo (BGC-Argo) floats have been developed (e.g., Claustre et al., 2020; Johnson et al., 2009, 2017; Pasqueron de Fommervault et al., 2015; Xing et al., 2011). Compared with the standard Argo floats which only carry conductivity-temperature-depth (CTD) sensors, BGC-Argo floats carry more biogeochemical sensors. These floats thus provide synchronous depth-resolved physical and biogeochemical data, which can be used for studying the physical-biological interactions (Chai et al., 2020; Claustre et al., 2020). Compared with the traditional shipboard observations, BGC-Argo floats often move along the currents at a certain depth and can achieve observations in a longer time with less cost. They sometimes observe the processes in multiple temporal (from days to years) and spatial scales (from submesoscale to basin scale) (Claustre et al., 2020). Meanwhile, because BGC-Argo often move along the currents for a long distance, there is a challenge to distinguish what mechanisms are responsible for the variability of the properties measured by them. In this study, through combining with some ancillary data, e.g., satellite observed absolute dynamic topography (ADT), sea surface temperature (SST), surface chlorophyll (CHL) and profiling data from some standard Argo floats, the influence of multi-scale dynamics on the nitrate distribution observed by two long-term (about 4 years for each) BGC-Argo floats around the KE is studied, with an emphasis on the potential influence of mesoscale eddies and their associated fronts. The information of the BGC-Argo floats and satellite data is described in Section 2. In Section 3, the influence of multi-scale dynamics on the nitrate distribution observed by the BGC-Argo floats is analyzed. The implications of the present study are discussed in Section 4, and the conclusions are presented in Section 5.

2. Data and methods

2.1. Float data

The two floats analyzed in the main text are numbered as 5904034 and 5904035, respectively, by the World Meteorological Organization (WMO). They both cycled from 1000 m depth to near the sea surface. Detailed temporal resolutions and cycled periods of the floats are given in Table 1. Their trajectories are shown in Fig. 1. From the year 2013 to 2017, Floats 5904034 and 5904035 moved between the subtropical and subpolar gyres and recorded vertical profiles of temperature, salinity, and nitrate concentration. Thus, the variations of the nitrate profiles measured by them are related to the influence of multi-scale dynamics, seasonal variability, and biological uptake. The data of Floats 5904034 and 5904035 are obtained from ftp://ftp.ifremer.fr/ifremer/argo, and only adjusted data are used in this study.

The vertical resolution of temperature and salinity is 2 m. The measurements of nitrate concentration are made at 60 depths (5 m resolution from surface to 100 m, 10 m resolution from 100 to 360 m, 20 m resolution from 360 to 400 m, and 50 m resolution from 400 to 1000 m). The nitrate concentration is observed using the optical nitrate sensors (In Situ Ultraviolet Spectrophotometer (ISUS)), which measure the seawater absorption spectrum in the wavelength range from 217 to 240 nm (Johnson & Coletti, 2002). The nitrate data processing and quality-control procedure include temperature-salinity correction (Sakamoto et al., 2009), pressure correction (Sakamoto et al., 2017), and offset adjustment (Johnson et al., 2013). The adjustment is based on the assumption that the bias of the ISUS sensor resulted from an initial calibration offset and a possible dark current drift over time and can be regarded as a constant offset for the entire profile (i.e., the offset correction) (Johnson et al., 2013). The adjustment procedure is to compare the raw float nitrate concentration to a reference estimate for nitrate in deep waters (e.g., 1000 m) where nitrate concentration is nearly constant. In this study, the nitrate data of Floats 5904034 and 5904035 have already been delayed-mode quality-controlled by the Monterey Bay Aquarium Research Institute (MBARI), using the same

Table 1
Information of the BGC-Argo floats 5904034 and 5904035. * The last profile represents the time of the last profiling data analyzed in this study.

WMO #	Date		Number of NO_3^- profiles	Time intervals among profiles
	First profile	Last profile*		
5904034	Mar. 1, 2013	Feb. 24, 2017	281	5 days
5904035	Mar. 2, 2013	Dec. 27, 2016	269	5 days

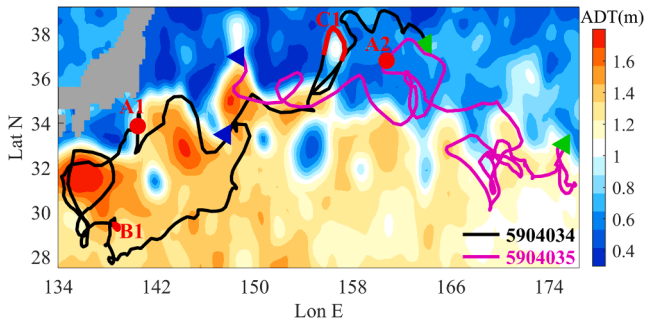

Fig. 1. Trajectories of Floats 5904034 and 5904035. Blue and green triangles indicate the initial and final locations of the floats, respectively. Background color indicates the snapshot of ADT on April 12, 2016, which is used to show the meanders and a substantial number of mesoscale eddies generated around the KE. The locations denoted with A1, A2, B1 and C1 indicate the locations during the corresponding dates shown in Fig. 2. (For interpretation of the references to color in this figure legend, the reader is referred to the web version of this article.)

procedures described in Johnson et al. (2017). After the drift adjustment, the nitrate data accuracy is expected to be improved to the order of 0.5 μmol kg^{-1} (Johnson et al., 2017). In addition to Floats 5904034 and 5904035, two other floats numbered as 2902754 and 2902755 are analyzed to support some conclusions of the present study, and their information and relevant results are shown in the supplementary material (supplementary Table S1, Figs. S1 and S2).

2.2. Ancillary data

Ancillary data used in this study include the following: multi-sensor-merged daily and 8-day composite 4-km-resolution surface CHL concentration fields downloaded from the Copernicus Marine Environment Monitoring Service (CMEMS, http://marine.copernicus.eu/); daily absolute dynamic topography (ADT), sea level anomaly (SLA) and surface horizontal geostrophic velocity fields with a spatial resolution of 0.25° downloaded from CMEMS, which are provided by the Archiving, Validation and Interpretation of Satellite Data in Oceanography (AVISO); daily sea surface temperature (SST) data with a spatial resolution of 0.01° obtained from the Jet Propulsion Laboratory (JPL) (https://coastwatch.pfeg.noaa.gov/erddap/griddap/jplMURSST41.html), which are based on microwave-derived SST, infrared-derived SST, and in-situ SST; monthly-climatology nitrate data with a spatial resolution of 1° obtained from the World Ocean Atlas 2013 (WOA13) (https://www.nodc.noaa.gov/cgi-bin/OC5/woa13/woa13oxnu.pl); standard Argo profiling data downloaded from ftp://ftp.ifremer.fr/ifremer/argo.

2.3. Quantification of MLD, N_{eu}, and strain rate

In the present study, the mixed layer depth (MLD) is defined as the depth where the seawater density increases by 0.03 kg m^{-3} relative to the reference depth of 10 m (de Boyer Montégut et al., 2004; Oka et al., 2007). We also analyzed the sensitivity of the results to different MLD definitions (e.g., with temperature threshold of 0.2 °C) and found insignificant influence on the main conclusions of the present study. The euphotic-layer averaged nitrate concentration (N_{eu}) is estimated with the vertically averaged nitrate concentration in the upper 100 m. We also estimated N_{eu} with the vertically averaged nitrate concentration in the upper 80 m and 120 m, respectively (supplementary Fig. S3), and found insignificant influence on the main results of the study.

Through using surface horizontal geostrophic velocity fields from the AVISO, the strain rate S induced by the geostrophic flow is calculated by

$$S = \sqrt{(\partial u_g/\partial x - \partial v_g/\partial y)^2 + (\partial v_g/\partial x + \partial u_g/\partial y)} \quad (1)$$

where (u_g, v_g) are the (x, y) components of the horizontal geostrophic flow at surface (Gula et al., 2014; Wang et al., 2021). Strain tends to compress fluid in one direction and stretch it in the perpendicular direction. When the direction of horizontal density gradient is perpendicular to the principle axis of strain rate, horizontal density gradients are enhanced to induce frontogenesis. The classical schematic diagram of strain field (or deformation flow) and its role in frontogenesis can refer to Fig. 9 in Klein and Lapeyre (2009) and Fig. 5 in McWilliams (2016).

3. Results

3.1. Relationship between nitrate profiles measured by the floats and ADT

The vertical profiles of potential temperature, salinity and nitrate concentration observed by the BGC-Argo floats are shown in Fig. 2. As shown in Fig. 1, the floats moved back and forth among the oligotrophic subtropical gyre, the KE and subpolar mesotrophic gyre. The KE is rich with mesoscale eddies, so the float-observed nitrate fields are likely to be influenced by several factors, such as the large-scale spatial heterogeneity, mesoscale eddies, submesoscale dynamics, seasonal variability, and biological uptake. Biological uptake mainly occurs in the euphotic layer. Under the euphotic layer, physical processes are likely to dominate the distribution of nitrate, which can be inferred from the similar patterns of potential temperature, salinity and nitrate concentration (Fig. 2b-2d and 2g-2i). As shown in Fig. 2d and 2i, nitrate concentration is better correlated with density than with depth. The correspondence of the vertical fluctuations of isopycnals and iso-nitrate surfaces primarily reflects that the physical dynamics induced vertical movements of iso-nitrate surfaces and isopycnals at the same time. In addition, because water movements in the ocean interior tend to follow density surfaces, the redistribution of isopycnal transport is also responsible for the correspondence of the density and nitrate concentration (Mahadevan, 2016). Nitrate concentration has also been shown to be more correlated with temperature or density than with depth in other studies (e.g., Ren et al., 2017).

The fluctuations of isopycnals and iso-nitrate surfaces are related to the variation of ADT along the trajectories of the floats (Fig. 2d-2e and 2i-2j). ADT with the resolution of 0.25° is a quantity that can resolve the influence of large- and meso-scale processes to some extent. Inside the subtropical gyre and most anticyclonic eddies, the sea surface is elevated to result in higher ADT than for surrounding waters, and isopycnals and iso-nitrate surfaces below the mixed layer are depressed relative to the surrounding water (McGillicuddy, 2016). Inside the subpolar gyre and most cyclonic eddies, the sea surface is depressed, resulting in lower ADT than for surrounding waters, and isopycnals and iso-nitrate surfaces are lifted up. As a result, the vertical fluctuations of isopycnals and iso-nitrate surfaces under the euphotic layer are roughly inversely proportional to ADT (Fig. 2d-2e and 2i-2j). In addition to the floats 5904034 and 5904035, we also analyzed two other BGC-Argo floats 2902754 and 2902755 around the KE, which moved within the subtropical and subpolar gyres, respectively (supplementary Figs. S1 and S2). They show similar relationship between the variations of iso-nitrate surfaces and isopycnals.

The depth-averaged nitrate concentrations (N_{eu}) in the eupthotic layer (0–100 m) measured by Floats 5904034 and 5904035 are shown in Fig. 2e and 2j. The variations of ADT and N_{eu} are negatively correlated. Through calculating all of the profiles obtained by the two BGC-Argo floats, the correlation coefficient between ADT and euphotic-layer nitrate concentration is quantified to be about −0.7 at the 95% confidence level. In addition to the vertical nitrate delivery forced by the large-scale and mesoscale processes, other processes (such as diapycnal mixing, seasonal variability, and biological uptake) also influence the relationship between nitrate concentration and density inside the euphotic layer; thus, the variations of ADT and N_{eu} show significant, though

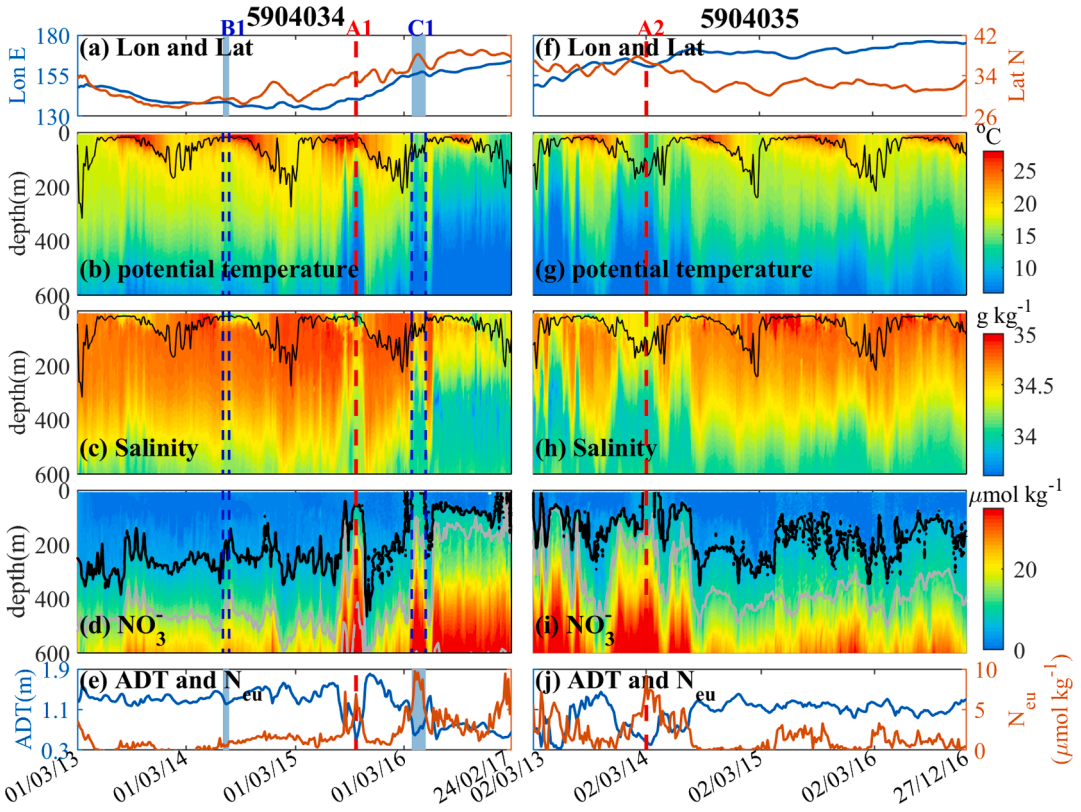

Fig. 2. Variations of (a) the latitudes and longitudes of the BGC-Argo float, profiles of (b) potential temperature, (c) salinity and (d) nitrate concentration measured by the float, and (e) ADT and N_{eu} along the trajectory of the float. Panels (a)-(e) and (f)-(j) show the results from Float 5904034 and 5904035, respectively. In panels (b), (c), (g) and (h), black lines indicate MLD. In panels (d) and (i), black lines indicate the iso-nitrate surface of $NO_3^- = 5\mu mol\ kg^{-1}$, and grey lines indicate the isopycnals with potential density of 1026 kg m^{-3}. In panels (e) and (j), blue lines indicate ADT at the corresponding time and locations along the trajectories of the floats, and orange lines indicate the vertical average of nitrate concentration in the euphotic zone (0–100 m) measured by the floats. The dates denoted with A1, A2, B1 and C1 indicate the dates of the cases analyzed in Figs. 3–7 and their corresponding locations are noted in Fig. 1. (For interpretation of the references to color in this figure legend, the reader is referred to the web version of this article.)

imperfect correlation. We have analyzed all profiles measured by the floats and their corresponding daily ADT, SLA, SST, CHL and geostrophic velocities, and two cases (on Dates A1 and A2) are chosen as examples to show how ADT is correlated to the nitrate distribution under the influence of large-scale dynamics in Section 3.2.

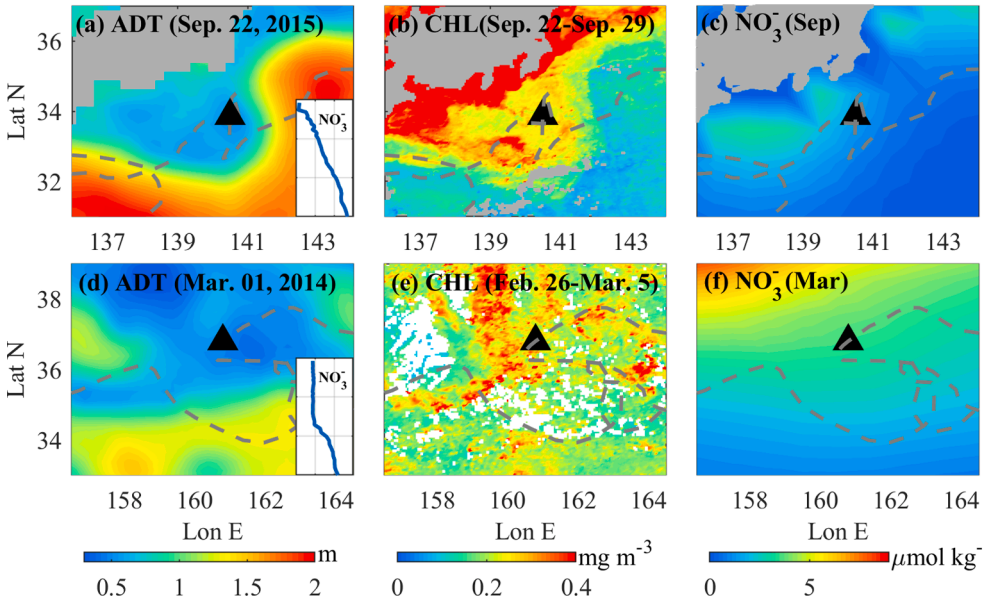

Fig. 3. Two cases for showing the relationships between ADT, nitrate concentration and surface CHL concentration under the influence of large-scale process. The cases shown in panels (a)-(c) and (d)-(f) correspond to Dates A1 and A2 in Fig. 2a and 2f, respectively. In panel (a), background colors and triangle indicate ADT and the location of the float on Date A1, respectively; Dashed line indicates the trajectory of Float 5904034; The blue line in the right bottom indicates the vertical profile of nitrate concentration on Date A1, whose vertical axis indicates depth in the range of 300–0 m, and horizontal axis indicates nitrate concentration in the range of 0 to 30 μmol kg^{-1}. Panel (b) indicates the surface CHL concentration during the time period which covered Date A1. Panel (c) shows the monthly-climatology mean nitrate concentration in the euphotic layer from WOA13. Panels (d)-(f) are similar to panels (a)-(c), but indicate Case A2. (For interpretation of the references to color in this figure legend, the reader is referred to the web version of this article.)

3.2. Influence of large-scale process on nitrate distribution measured by the floats

The large-scale process results in spatial heterogeneity of the depth of isopycnals and iso-nitrate surfaces between the north and south sides of the KE. When the floats moved across the KE, the depth of iso-nitrate surfaces those they measured changed a lot. Fig. 3 shows the two cases with elevated nitrate concentration on Dates A1 and A2, when the corresponding ADT was low and iso-nitrate surfaces were uplifted (Fig. 2d, 2e, 2i, and 2j). On Date A1, Float 5904034 moved inside the subpolar waters near the coast of Japan, where ADT was lower than its surrounding water (Fig. 3a). The low ADT resulted from the Kuroshio meander formed on the south side of Japan (Chang et al., 2019). Both the up-lifted iso-nitrate surfaces in the background subpolar water and coastal water supplied abundant nitrate into the euphotic layer, benefiting high CHL concentration (Fig. 3b). The monthly-mean climatology of nitrate concentration from WOA13 roughly shows the influence of this meander on the euphotic-layer nitrate concentration (Fig. 3c), but its magnitude is lower than that measured by the BGC-Argo Float 5904034 (6.9 μmol kg^{-1}) due to the inter-annual variability of the meander (Guo et al., 2019).

In the profiles measured by Float 5904035, iso-nitrate surfaces were uplifted around Date A2 (Fig. 2i). During that time, the float moved into the subpolar water with low ADT (Fig. 3d), and the uplifted iso-nitrate surfaces supplied nitrate into the euphotic layer to support high CHL concentration (Fig. 3e). This influence of the large-scale process is reflected by the monthly-mean climatology of nitrate concentration from WOA13, with lower ADT corresponding to higher nitrate concentration (Fig. 3d and 3f). The magnitude of monthly climatology mean nitrate concentration is comparable to that measured by the float (about 9 μmol kg^{-1}).

3.3. Potential influence of a cyclonic mesoscale eddy in the subtropical gyre

In addition to the large-scale dynamics, the fluctuations of iso-nitrate surfaces under the euphotic layer are likely to be influenced by mesoscale eddies, as shown in the following case during Period B1. As shown in Fig. 4a and 4b, from June 27 to July 7, 2014, Float 5904034 (pink triangles) moved into a westward propagating cyclonic mesoscale eddy from outside. As Float 5904034 moved from outside into the eddy, the subsurface (from 80 m to 300 m) temperature observed by it decreased (as shown with the solid blue and green lines in Fig. 4d), while the subsurface nitrate concentration increased (as shown with the solid blue and green lines in Fig. 4e). This implied that the subsurface isopycnals and iso-nitrate surfaces were up-lifted inside the eddy. From July 7 to July 12, Float 5904034 continued moving toward the core of the eddy (Fig. 4b and 4c), and the subsurface nitrate concentration increased a little more slightly (as shown with the solid green and red lines in Fig. 4e).

To identify that the variations of temperature and nitrate concentration measured by Float 5904034 were mainly due to the local influence of the mesoscale eddy, we searched for more standard Argo floats which were the nearest to Float 5904034 in the same dates (black dots in Fig. 4a-4c). Although these standard Argo floats did not carry nitrate sensors, the temperature profiles measured by them could reflect whether there was significant influence of large-scale water mass exchange or wind-induced Ekman pumping near the mesoscale eddy during Period B1 to some extent. The temperature profiles observed by these standard Argo floats showed that there was no significant decrease of subsurface temperature outside of the eddy from June 27 to July 12 (dashed lines in Fig. 4d). On June 27, Floats 5904034 and 2901566 were both outside the eddy (Fig. 4a), and the temperature profiles measured by them were close to each other (Fig. 4c). On July 7 and 12, the temperature profiles measured by Floats 5904034 and 2901552 exhibited significant difference, which was likely due to the influence of the eddy. This implied that the variations of subsurface temperature and nitrate concentration measured by Float 5904034 during Period B1 were potentially due to the influence of the cyclonic eddy.

Although the subsurface nitrate concentration measured by Float 5904034 increased during Period B1, there was no significant variability of the nitrate concentration in the upper 80 m (Fig. 4e). We speculate that it is because that the upwelled nitrate was hindered by the seasonal thermocline (Fig. 4d). In the present study, the bottom of the seasonal thermocline is defined as the depth where the temperature gradient is first smaller than 0.02 °C m^{-1}. The depth of the seasonal thermocline from the three profiles measured by Float 5904034 was about 120 m (June 27), 96 m (July 7), and 86 m (July 12), respectively. These

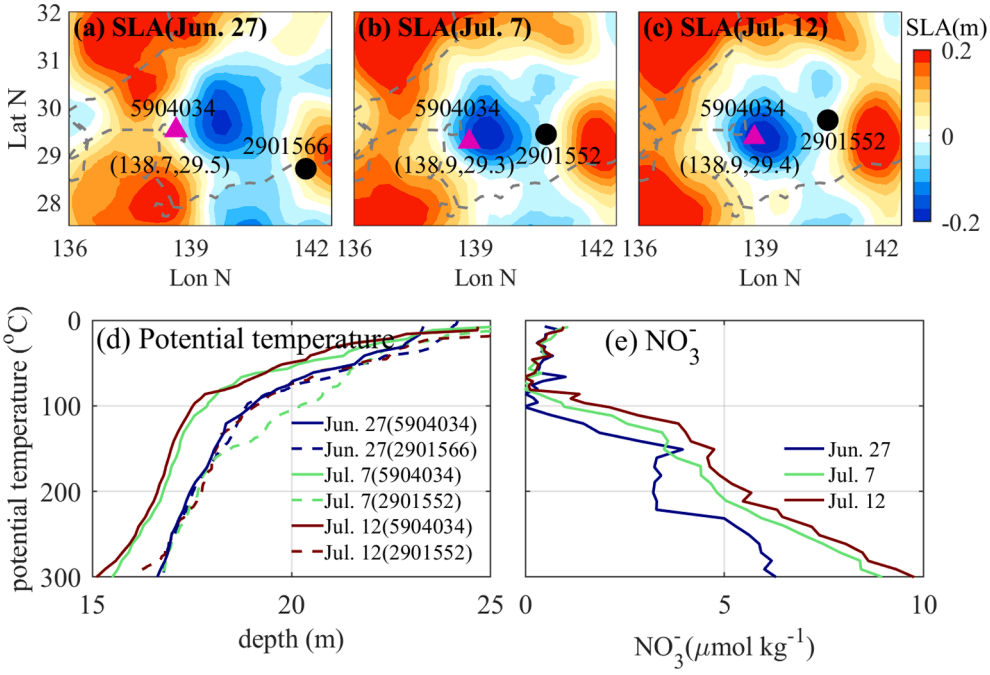

Fig. 4. Influence of a mesoscale eddy on the vertical profiles of temperature and nitrate concentration measured by Argo floats. In panels (a)-(c), background colors indicate SLA. Pink triangles and black dots indicate the locations of Float 5904034 and some standard Argo floats which were the nearest to Float 5904034 in the same dates, respectively. The numbers in the bracket under the triangles indicate the longitudes and latitudes of the triangles. Dashed line indicates the trajectory of Float 5904034. Solid lines in panels (d) and (e) indicate the vertical profiles of potential temperature and nitrate concentration in the upper 300 m measured by Float 5904034, respectively. Dashed lines in panel (d) indicate the vertical profiles of potential temperature measured by the standard Argo floats which were the nearest to Float 5904034 in the same dates. (For interpretation of the references to color in this figure legend, the reader is referred to the web version of this article.)

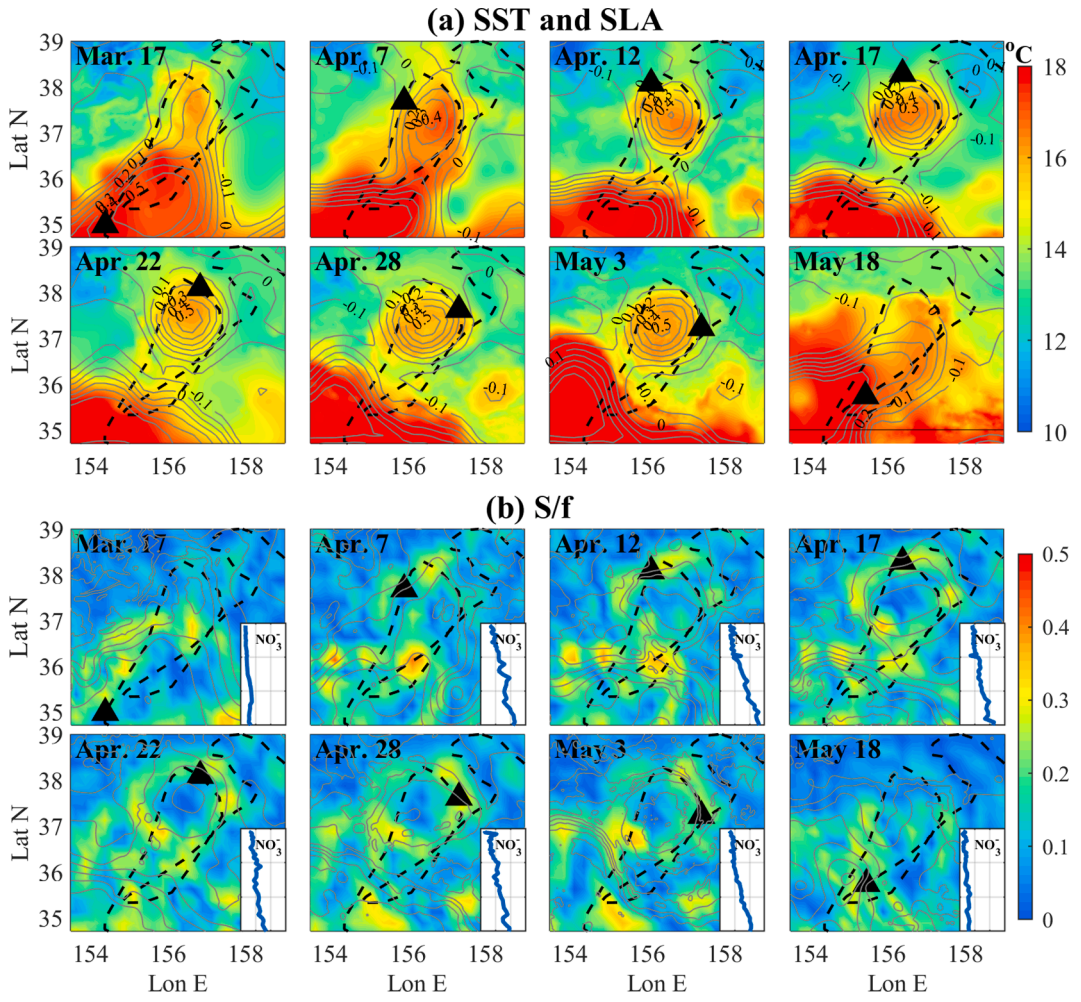

Fig. 5. Snapshots of SST, SLA and strain rate S normalized by f during Period C1. Dashed line indicates the trajectory of Float 5904034, and triangles indicate the locations of the float at the corresponding dates. In panel (a), colors indicate SST and grey contours indicate SLA with unit of m. In panel (b), colors indicate the magnitude of strain rate S normalized by f, and grey contours indicate SST with interval of 1 °C; The blue lines in the right bottom of each panel indicate the vertical profiles of nitrate concentration measured by Float 5904034, whose vertical axis indicates depth in the range of 300–0 m, and horizontal axis indicates nitrate concentration in the range of 0–30 μmol kg^{-1}. (For interpretation of the references to color in this figure legend, the reader is referred to the web version of this article.)

roughly corresponded to the depth where the nitrate concentration began to be larger 1 μmol kg^{-1}, which was about 120 m (June 27), 101 m (July 7), and 86 m (July 12), respectively.

During Period B1, Float 5904034 moved inside the oligotrophic subtropical region (Fig. 1). Case B1 shows that a westward propagating cyclonic eddy upwelled nitrate in the subsurface, but it did not supply much nitrate into the surface layer possibly due to the inhibition of thermocline during summer. This might enhance the primary production from 80 m to the bottom of the euphotic layer, while did not enhance the primary production at surface. Correspondingly, there was no apparent elevation of surface CHL from the satellite data (surface CHL was lower than 0.2 mg m^{-3}) around the eddy during Period B1 (not shown for brevity). Although Case B1 can not represent the situations of all cyclonic eddies, it shows the possibility that some cyclonic eddies upwelled nitrate in the subsurface, while did not supply much nitrate into the surface layer due to the inhibition of seasonal thermocline in the subtropical Northwestern Pacific Ocean during summer.

3.4. Potential influence of submesoscale process around an anti-cyclonic eddy

3.4.1. Elevated nitrate concentration along the periphery of an anti-cyclonic eddy

In addition to the apparent influence of large-scale and mesoscale dynamics, the distributions of nitrate and CHL are also related to the processes in smaller scales. An examination of the trajectories of Float 5904034 shows that it moved along the periphery of an anti-cyclonic mesoscale eddy during Period C1, as discussed in analysis that follows. The corresponding locations of the float and time period of Case C1 for analysis are noted in Figs. 1 and 2, respectively.

During Period C1 (March 22 - May 13, 2016), isopycnals and isonitrate surfaces were uplifted (Fig. 2d). Correspondingly, there was a peak of nitrate concentration in the euphotic zone (Fig. 2e). The distributions of ADT and SST (Fig. 5a) showed a warm, anticyclonic mesoscale eddy being detached from the KE, and Float 5904034 moved along the KE front and the periphery of the mesoscale eddy. Eleven profiles have been recorded by the float during Period C1, and six of them are shown in Fig. 5. During Period C1, MLD differed much from that observed before and after Period C1 (Fig. 2b). Before and after moving along the KE front and the periphery of the mesoscale eddy, the nitrate concentrations measured by Float 5904034 were both much lower than

those measured during Period C1, as shown with the nitrate profiles in Fig. 5b. This implied that a very limited quantity of nitrate was trapped inside the eddy. One potential mechanism for the elevation of nitrate concentration was the upwelling induced by submesoscale dynamics along the periphery of the eddy, as explained in the following.

Fig. 5b shows that relatively strong strain occurred along the periphery of the mesoscale eddy. When the direction of horizontal density gradient is perpendicular to the principle axis of strain rate, isopycnals are often compressed to enhance the frontal sharpness. Along the periphery of the mesoscale eddy, isotherms were compressed to be close to each other (Fig. 5b). According to the discussions in some previous studies (e.g., Mahadevan, 2016; McWilliams, 2016), ageostrophic secondary circulations are often induced in the cross-front direction, which may drive nutrients up into the euphotic layer to support CHL. Therefore, our hypothesis for the potential mechanism is that when the warm eddy moved inside the subpolar water during Period C1, the submeoscale processes along its periphery upwelled high subsurface nitrate concentration into the euphotic layer (Fig. 5b).

Through using high-resolution numerical models (with horizontal resolution of 500 m), Luo et al. (2020) simulated the submesoscale dynamics of a similar anti-cyclonic eddy that was detached from the KE. They found significant secondary circulations along the periphery of the eddy. Although they did not simulate nutrients, the secondary circulations in their simulations supported our hypothesis that the ageostrophic circulations were one important potential mechanism to upwell nutrients along the periphery of anti-cyclonic eddies on the northern edge of the KE. In addition to the local submesoscale process, there were also other potential mechanisms, including the horizontal advection from the surrounding subpolar water, surface cooling, wind-induced mixing and Ekman pumping. To examine whether there was significant local influence of the mesoscale eddy on the elevated nitrate concentration, some further analysis is shown as follows.

There was no synchronous observations of nitrate outside of the eddy during Period C1, so there was no direct evidence to identify that the elevated nitrate concentration was not totally horizontally advected from the surrounding subpolar water or due to wind-induced mixing. However, some indirect analysis could provide some clues. Firstly, we found some standard Argo floats whose locations were close to Float 5904034 during the same dates, and compared the profiles of temperature and salinity measured by them (Fig. 6). On April 12, Float 5,904,090 was in the subpolar water and close to Float 5904034 (Fig. 6a). The temperature and salinity profiles measured by Float 5904034 along the periphery of the eddy were much different from that measured by Float 5904090, with surface temperature and salinity difference about 3 °C and 0.2 g kg^{-1}, respectively. This implied that there was significant difference between the properties measured by Floats 5904034 and 5904090. In addition, MLD along the periphery of the eddy was deeper than the subpolar water, which was possibly related to the enhanced mixing at the fronts (D'Asaro et al., 2011; Yang et al., 2017). The comparison of Floats 5904034 and 2901681 showed similar results. The significant temperature and salinity difference between the profiles along and outside the eddy indicated the local effects of the eddy on the distributions of properties (e.g., temperature, salinity and nitrate) to some extent. Secondly, the monthly-climatology euphotic-layer averaged nitrate concentration during April (about 4 μmol kg^{-1}) was much lower than that measured by Float 5904034 (about 8 μmol kg^{-1}) in the same region (supplementary Fig. S4), indicating the potential influence of the mesoscale eddy or other inter-annual variability during Period C1. Thirdly, after Period C1, the euphotic-layer nitrate concentration measured by Float 5904034 was much lower than that during Period C1 until the last 8 profiles (Fig. 2e), although the float moved at higher latitudes for about eight months (Fig. 1 and supplementary Fig. S4). In the last 8 profiles, the elevated nitrate concentration (Fig. 2d and 2e) was related to winter mixing and another eddy (supplementary Fig. S5). In all of the profiles measured by Floats 5904034 and 5904035, the occurrence of such high nitrate concentration (about 8 μmol kg^{-1}) in April was only found during Period C1. All of the above analyses do not totally exclude the influence of the horizontal advection from the surrounding subpolar water, but they imply that the mesoscale eddy had local effects to some extent.

We also analyzed the temporal variations of local wind, sea surface net heat flux, and wind-induced Ekman pumping from March 1 to May

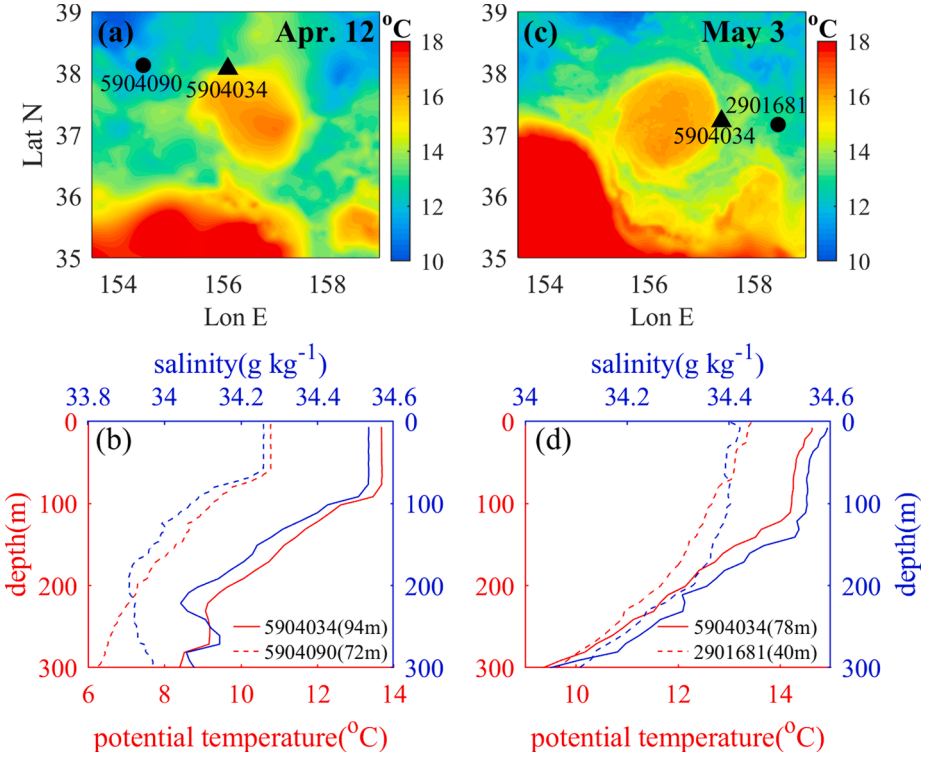

Fig. 6. Temperature and salinity profiles measured by different Argo floats in the same dates. (a) Triangle and dot indicate the locations of Floats 5904034 and 5904090 on April 12, 2016, respectively. Background colors indicate SST. (b) Solid lines indicate the potential temperature and salinity profiles measured by Float 5904034, and dashed lines indicate those measured by Float 5904090. The numbers inside the brackets indicate MLD of the corresponding profiles. Panels (c) and (d) are similar to (a) and (b), but for Floats 5904034 and 2901681 on May 3, 2016.

31 in 2016 (supplementary Fig. S6), and did not find significant correlation between them with the elevated nitrate concentration during Period C1. In addition, being different from the case shown in supplementary Fig. S5, there was no significant temporal variability of SST inside the mesoscale eddy (Fig. 5a), implying that there was no significant surface cooling during Period C1. We also calculated the anomaly of N_{eu} through removing the monthly NO_3^- (WOA13) from the BGC-Argo observed NO_3^- (supplementary Fig. S7). The anomaly of N_{eu} showed a peak during Period C1, indicating the potential influence of the mesoscale eddy or other inter-annual variability.

According to the above analyses, the elevated nitrate concentration during Period C1 was not totally horizontally advected from the surrounding water, and the wind-induced mixing, Ekman pumping and sea surface net heat flux did not seem to have significant effects. The correspondence between strain rate, compressed isotherms, and elevated nitrate concentration along the periphery of the eddy indicates the potential influence of submesoscale dynamics.

3.4.2. Relationship between the elevated nitrate concentration and surface CHL

In the subpolar region, nitrate may not be the limiting nutrient for CHL, but the vertical delivery of nitrate indicates the same process could have occurred for other limiting nutrients, such as iron. The supply of nutrients from deep water may enhance the CHL at surface. This was corresponding to the satellite-observed ring of elevated CHL concentration along the periphery of this eddy (Fig. 7). In addition to the supply of nutrients from deep water, the horizontal advection certainly had effects on the distribution of surface CHL. To examine the effects of horizontal geostrophic advection on the distribution of surface CHL, we performed the eddy's transport properties through a numerical experiment. In the numerical experiment, we computed the trajectories of synthetic particles initiated on April 30 and advected by the satellite derived daily geostrophic velocity fields. The particles were initiated at the regions with CHL concentration greater than 0.45 mg m^{-3} on April 30, 2016 (Fig. 7c). Trajectories used for Lagrangian analysis were computed by integrating the geostrophic velocities with a time step of 1 h. The final locations of the particles on May 4 are shown in Fig. 7d. As shown in Fig. 7d, some particles were advected along the periphery of the mesoscale eddy, while they only occupied a small part of the area where the CHL concentration was greater than 0.45 mg m^{-3} on May 4. This implied that geostrophic horizontal advection had effects on the elevated CHL concentration along the periphery of this eddy, but it could not explain all of the new production of CHL on May 4. The numerical tracking with the daily velocity fields certainty had some bias, but the advected distances of the particles in the northeastern side of the ring was much shorter than the real length of the ring with CHL concentration greater than 0.45 mg m^{-3} on May 4, 2016.

The horizontal confluent flow and ageostrophic convergence also possibly had effects on structuring the ring of the elevated CHL. However, both of the confluence and convergence are relevant to the submesoscale dynamics, which tended to induce vertical secondary circulations at the same time. As discussed in Mahadevan (2016) and Lehahn (2018), the vertical and horizontal dynamics of submesoscale processes are intrinsically linked. Considering the synchronous occurrence of elevated nitrate concentration along the periphery of the eddy, the upwelling of nutrients induced by submesoscale dynamics also likely played important roles in supporting the elevated surface CHL, in addition to the horizontal transports.

4. Discussions

4.1. Another case with elevated CHL around the periphery of mesoscale eddies

The ring of elevated CHL also occurred in some other eddies in this area, such as the eddy shown in Fig. 8. A warm, anticyclonic eddy was detached from the southwest region shown in Fig. 8, and along the periphery of this eddy, a CHL ring was formed (Fig. 8f). As shown in Fig. 8e, the CHL ring was located inside the warm eddy, so CHL concentration was low in the original region where the eddy was formed. In addition, the ring of CHL was isolated by the surrounding water (Fig. 8f), which was similar to Case C1 to some extent (Fig. 7). Similar to Section 3.4, we suggest that the upwelling of nutrients along the periphery of the eddy played a significant role in supporting the surface high CHL.

The new production of CHL along the ring was not likely horizontally stirred from the northwestern high CHL concentration region in Fig. 8c. Compared with the part of the CHL ring shown on June 2 (Fig. 8c), CHL concentration along the ring on June 4 was higher (Fig. 8f). Even with the maximum horizontal velocities (about 1 m s^{-1}), the advected distance would have been about 173 km from June 2 to June 4, which was not long enough to advect the CHL from the northwestern region into the northern part of the ring. Therefore, vertical processes likely had effects on the new production of CHL along the ring from June 2 to June 4. Unfortunately, there was no observation of nutrients profiles along this eddy.

4.2. Implications of BGC-Argo observations for the study of physical-biological interactions around the KE

Around the KE, surface CHL usually exhibits multi-scale patterns, as shown in the satellite views in Fig. 9a. In the large-scale, lower ADT (Fig. 9b) roughly corresponds to higher concentration of surface CHL, such as the northwestern region (37-42°N, 135–155°E) shown in Fig. 9a.

As shown in Fig. 9a and stated in Naigai et al. (2019), the CHL

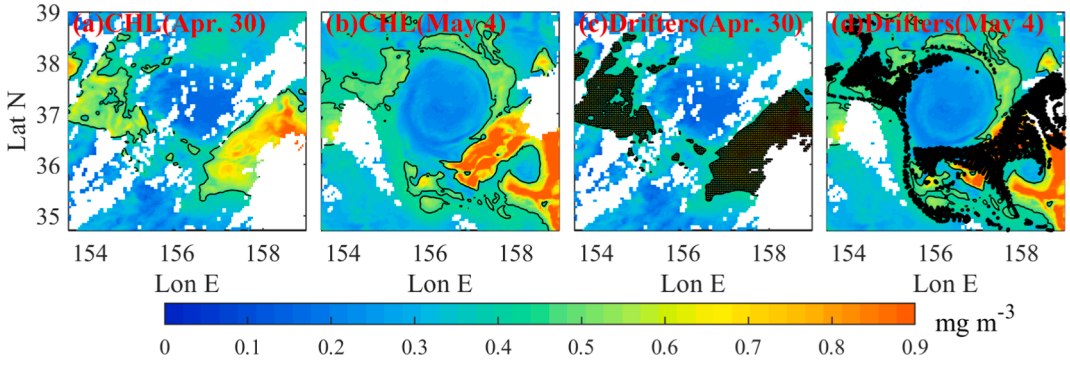

Fig. 7. Distributions of daily surface CHL concentrations on April 30 and May 4, 2016. Black contours in each panel indicate the isoline of CHL with concentration of 0.45 mg m^{-3}. Panels (c) and (d) show the trajectories of synthetic numerical particles advected by the satellite derived velocity field (black dots) from April 30 to May 4. The synthetic numerical particles were selected as the pixels with CHL concentration greater than 0.45 mg m^{-3} on April 30. White regions indicate missing data due to cloud cover.

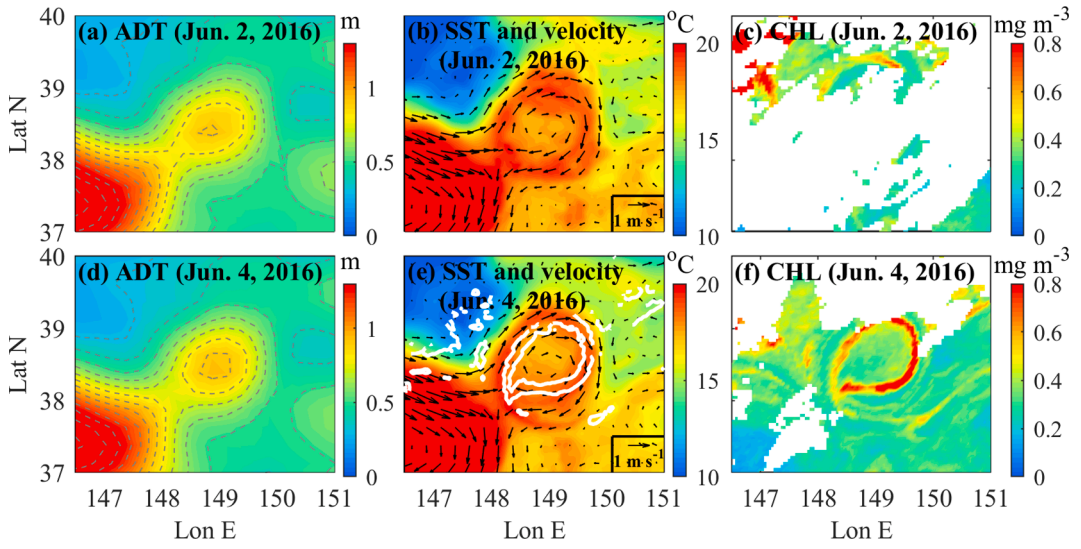

Fig. 8. A case with high CHL concentration along the periphery of a mesoscale eddy. In panels (b) and (e), arrows indicate the daily surface geostrophic velocities. In panel (e), white contours indicate the isoline with CHL concentration of 0.45 mg m^{-3}, which are used to denote the position of the CHL ring. In panels (c) and (f), white regions indicate missing data due to clouds.

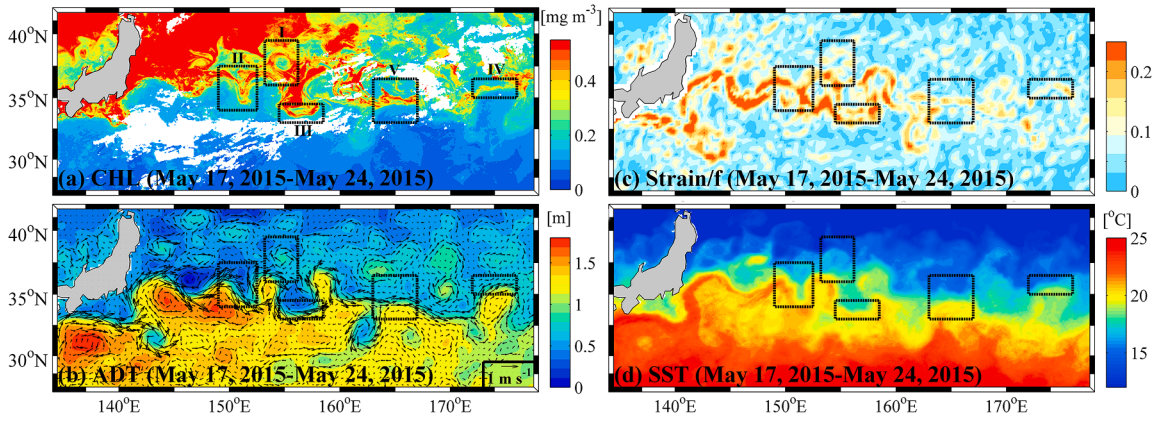

Fig. 9. Relationships between the (a) eight-day composite sea surface chlorophyll (CHL) concentration, eight-day averaged (b) absolute dynamical topography (ADT, color) with geostrophic velocities (arrows) overlaid, (c) strain rate normalized by the Coriolis frequency f (Strain/f), and (d) sea surface temperature (SST) in the Kuroshio Extension region during May 17–24, 2015. In Panel (a), white areas indicate missing data due to cloud cover. Black boxes indicate the cases where the width of CHL hotpots was on the order of 10 km.

concentrations are substantially elevated along the northern edge of the KE (35–37°N, 145–180°E) during spring, but lower in adjacent regions further north. Up to now, it is still not clear why CHL concentrations ars elevated along the northern edge of the KE. As shown with the black boxes in Fig. 9a, the elevated CHL concentrations are sometimes in the shape of strips or rings with spatial scales of 10 km, and are apparently related to the horizontal gradients of ADT (Fig. 9b). Under geostrophic balance, a strong horizontal gradient of ADT corresponds to strong geostrophic currents (Fig. 9b). Thus one potential explanation for the elevated CHL associated with the northern flank of the KE is the horizontal advection of nutrients and CHL from the coastal and northwestern waters (Fig. 9a and 9b). Meanwhile, in the regions with strong geostrophic currents (e.g., along the KE front and the periphery of mesoscale eddies), high strain rate is often induced (Fig. 9c). As discussed in Section 3.4, when the direction of horizontal density gradient is perpendicular to the principle axis of strain rate, fronts and filaments are often generated (Fig. 9d). The ageostrophic secondary circulations in the cross-front direction may drive nutrients up into the euphotic layer to support CHL.

The vertical supply of nutrients is closely related to the horizontal shear and vorticity of the flow, so it is hard to identify whether there is vertical supply of nutrients in the regions with elevated CHL only through the satellite data. The present study shows a case that nitrate concentration was elevated along the periphery of a warm eddy on the northern side of the KE. Combing with further analysis, we suggest the possibility that submesoscale processes in the upper layers of the fronts and eddies supply nutrients into the euphotic layer. Because the KE region is rich of warm mesoscale eddies, fronts and filaments, it is likely that the submesoscale processes play a significant role in the vertical supply of nutrients to support the elevated CHL along the northern edge of the KE.

In addition to the mechanism for the elevated CHL along the northern edge of the KE, another notwell-understood topic is how nitrate is supplied into the euphotic layer to support primary production in the subtropical ocean during spring and summer (Johnson et al., 2010). Johnson et al. (2010) has shown episodic subsurface nitrate upwelling around a cyclonic eddy near the Hawaii Ocean (Fig. 3 in Johnson et al. (2010)). In the present study, we show a case that subsurface nitrate concentration was elevated due to the influence of a cyclonic mesoscale eddy in the subtropical Northwestern Pacific Ocean during summer. Due to the inhibition of seasonal thermocline, nitrate was hard to be upwelled into the surface layer inside this eddy.

5. Conclusions

In this study, the influence of multi-scale dynamics on the vertical distribution of nitrate concentration measured by two BGC-Argo floats around the KE region is investigated. The temporal variation of the float-observed nitrate concentration is positively correlated with density, and negatively correlated with ADT. In the subtropical Northwestern Pacific Ocean, subsurface nitrate concentration was found to be elevated inside a cyclonic eddy. Possibly due to the inhibition of seasonal thermocline, nitrate was hard to be upwelled into the surface layer inside this eddy. Along the northern edge of the KE, the synchronous occurrence of elevated euphotic-layer nitrate and surface CHL concentrations was observed along the periphery of a warm and anti-cyclonic eddy. Through combining with some further analysis, we suggest that the upwelling induced by the submesoscale dynamics was likely a significant mechanism for supplying nutrients into the euphotic layer and supporting CHL along periphery of the anti-cyclonic eddy.

In both of the subtropical ocean and the northern edge of the KE, it is not well-understood how nutrients are supplied into the euphotic layer and support primary production. The present study reports two cases those are relevant to mesoscale and submesoscale dynamics, respectively. With more deployments of BGC-Argo floats and surface drifters equipped with chemical and biological sensors, the influences of mesoscale and submesoscale dynamics on biogeochemical processes around the KE region would become clearer.

Declaration of Competing Interest

The authors declare that they have no known competing financial interests or personal relationships that could have appeared to influence the work reported in this paper.

Acknowledgments

This study is supported by the National Key Research and Development Program of China [2016YFC1401600], the National Natural Science Foundation of China [42076006, 41730536, and 41876032], the Open Research Fund of the State Key Laboratory of Satellite Ocean Environment Dynamics [QNHX1815], the Marine S&T Fund of Shandong Province for Pilot National Laboratory for Marine Science and Technology (Qingdao) [2018SDKJ0206], and the Qingdao National Laboratory for Marine Science and Technology [QNLM2016ORP0103]. We would like to acknowledge the reviewers for their insightful suggestions on improving the manuscript. All Argo data are available on the GDAC FTP servers (http://doi.org/10.17882/42182 & ftp://ftp.ifremer.fr/ifremer/argo/)

Appendix A. Supplementary material

Supplementary data to this article can be found online at https://doi.org/10.1016/j.pocean.2021.102543.

References

Barkan, R., McWilliams, J.C., Shchepetkin, A.F., Molemaker, M.J., Renault, L., Bracco, A., Choi, J., 2017. Submesoscale dynamics in the Northern Gulf of Mexico. Part I: regional and seasonal characterization and the role of river outflow. J. Phys. Oceanogr. 47, 2325–2346. https://doi.org/10.1175/JPO-D-17-0035.

Barkan, R., Molemaker, M.J., Srinivasan, K., McWilliams, J.C., D'Asaro, E.A., 2019. The role of horizontal divergence in submesoscale frontogenesis. J. Phys. Oceanogr. 49, 1593–1617. https://doi.org/10.1175/JPO-D-18-0162.1.

Brannigan, L., 2016. Intense submesoscale upwelling in anticyclonic eddies. Geophys. Res. Lett. 43, 3360–3369. https://doi.org/10.1002/2016GL067926.

Calil, P.H.R., Richards, K.J., 2010. Transient upwelling hot spots in the oligotrophic North Pacific. J. Geophys. Res.-Oceans 115, C02003. https://doi.org/10.1029/2009JC005360.

Capet, X., McWilliams, J.C., Molemaker, M.J., Shchepetkin, A.F., 2008. Mesoscale to submesoscale transition in the California Current System. Part II: Frontal processes. J. Phys. Oceanogr. 38, 44–64. https://doi.org/10.1175/2007JPO3672.1.

Chai, F., Johnson, K.S., Claustre, H., Xing, X., Wang, Y., Boss, E., Riser, S., Fennel, K., Schofield, O., Sutton, A., 2020. Monitoring ocean biogeochemistry with autonomous platforms. Nat. Rev. Earth Environ. 1, 315–326. https://doi.org/10.1038/s43017-020-0053-y.

Chang, Y.-L.K., Miyazawa, Y., Miller, M.J., Tsukamoto, K., 2019. Influence of ocean circulation and the Kuroshio large meander on the 2018 Japanese eel recruitment season. PLoS ONE 14 (9), e0223262. https://doi.org/10.1371/journal.pone.0223262.

Chelton, D.B., Gaube, P., Schlax, M.G., Early, J.J., Samelson, R.M., 2011. The influence of nonlinear mesoscale eddies on near-surface oceanic chlorophyll. Science 334, 328–332. https://doi.org/10.1126/science.1208897.

Claustre, H., Johnson, K.S., Takeshita, Y., 2020. Observing the global ocean with biogeochemical-argo. Ann. Rev. Mar. Sci. 12, 23–48. https://doi.org/10.1146/annurev-marine-010419-010956.

Cronin, M.F., Meinig, C., Sabine, C.L., Ichikawa, H., Tomita, H., 2008. Surface mooring network in the Kuroshio extension. IEEE Syst. J. 2, 424–430. https://doi.org/10.1109/JSYST.2008.925982.

D'Asaro, E., Lee, C., Rainville, L., Harcourt, R., Thomas, L., 2011. Enhanced turbulence and energy dissipation at ocean fronts. Science 332, 318–322. https://doi.org/10.1126/science.1201515.

de Boyer Monté gut, C., Madec, G., Fischer, A.S., Lazar, A., Iudicone, D., 2004. Mixed layer depth over the global ocean: An examination of profile data and a profile-based climatology. J. Geophys. Res., 109, C12003, doi:10.1029/2004JC002378.

Fassbender, A.J., Sabine, C.L., Cronin, M.F., Sutton, A.J., 2017. Mixed-layer carbon cycling at the Kuroshio extension observatory. Global Biogeochem. Cycles 31, 272–288. https://doi.org/10.1002/2016GB005547.

Gaube, P., Chelton, D.B., Strutton, P.G., Behrenfeld, M.J., 2013. Satellite observations of chlorophyll, phytoplankton biomass, and Ekman pumping in nonlinear mesoscale eddies. J. Geophys. Res.-Oceans 118, 6349–6370. https://doi.org/10.1002/2013JC009027.

Gula, J., Molemaker, M.J., McWilliams, J.C., 2014. Submesoscale cold filaments in the Gulf Stream. J. Phys. Oceanogr. 44, 2617–2643. https://doi.org/10.1175/JPO-D-14-0029.1.

Guo, X.Y., Zhu, X.-H., Long, Y., Huang, D.J., 2013. Spatial variations in the Kuroshio nutrient transport from the East China Sea to south of Japan. Biogeosciences 10, 6403–6417. https://doi.org/10.5194/bg-10-6403-2013.

Guo, X.Y., Hu, Y., Sasai, Y., 2019. Contribution of Kuroshio recirculation to nutrient transport along the Kuroshio South of Japan: an analysis of model results. In: Nagai, T., Saito, H., Suzuki, K., Takahashi, M. (Eds.), Kuroshio current physical, biogeochemical, and ecosystem dynamics (Geophysical Monograph Series Book 243). AGU-Wiley, NJ, pp. 127–135.

Hosegood, P.J., Nightingale, P.D., Reesb, A.P., Widdicombe, C.E., Woodward, E.M.S., Clark, D.R., Torres, R.J., 2017. Nutrient pumping by submesoscale circulations in the Mauritanian upwelling system. Prog. Oceanogr. 159, 223–236. https://doi.org/10.1016/j.pocean.2017.10.004.

Jenkins, W.J., 1988. Nitrate flux into the euphotic zone near Bermuda. Nature 331, 521–523. https://doi.org/10.1038/331521a0.

Johnson, K.S., Coletti, L.J., 2002. In situ ultraviolet spectrophotometry for high resolution and long-term monitoring of nitrate, bromide and bisulfide in the ocean. Deep Sea Res. I 49, 1291–1305.

Johnson, K.S., Berelson, W.M., Boss, E.S., Chase, Z., Claustre, H., Emerson, S.R., Gruber, N., Kortzinger, A., Perry, M.J., Riser, S.C., 2009. Observing biogeochemical cycles at global scale with profiling floats and gliders: prospect for a global array. Oceanography 22, 216–225. https://doi.org/10.5670/oceanog.2009.81.

Johnson, K.S., Riser, S.C., Karl, D.M., 2010. Nitrate supply from deep to near-surface waters of the North Pacific subtropical gyre. Nature 465, 1062–1065. https://doi.org/10.1038/nature09170.

Johnson, K.S., Coletti, L., Jannasch, H., Sakamoto, C., Swift, D., Riser, S., 2013. Long-term nitrate measurements in the ocean using the in situ ultraviolet spectrophotometer: Sensor integration into the apex profiling float. J. Atmos. Oceanic Technol. 30, 1854–1866. https://doi.org/10.1175/JTECH-D-12-00221.1.

Johnson, K.S., Plant, J.N., Dunne, J.P., Talley, L.D., Sarmiento, J.L., 2017. Annual nitrate drawdown observed by SOCCOM profiling floats and the relationship to annual net community production. J. Geophys. Res. 122, 6668–6683. https://doi.org/10.1002/2017JC012839.

Kahru, B., Mitchell, G., Gille, S.T., Hewes, C.D., Holm-Hansen, O., 2007. Eddies enhance biological production in the Weddell scotia confluence of the southern Ocean. Geophys. Res. Lett. 34 (14), 116–130. https://doi.org/10.1029/2007gl030430.

Klein, P., Lapeyre, G., 2009. The oceanic vertical pump induced by mesoscale and submesoscale turbulence. Ann. Rev. Mar. Sci. 1, 351–375. https://doi.org/10.1146/annurev.marine.010908.163704.

Lehahn, Y., d 'Ovidio, F., Koren, I., 2018. A satellite-based lagrangian view on phytoplankton dynamics. Ann. Rev. Mar. Sci., 10, 99-119. doi: https://doi.org/10.1146/annurev-marine-121916-063204.

Lévy, M., Ferrari, R., Franks, P.J.S., Martin, A.P., Rivière, P., 2012. Bringing physics to life at the submesoscale. Geophys. Res. Lett. 39, L14602. https://doi.org/10.1029/2012GL052756.

Li, Y., He, R., 2014. Spatial and temporal variability of SST and ocean color in the Gulf of Maine based on cloud-free SST and chlorophyll reconstructions in 2003–2012. Remote Sens. Environ. 144, 98–108. https://doi.org/10.1016/j.rse.2014.01.019.

Liu, X., Levine, N.M., 2016. Enhancement of phytoplankton chlorophyll by submesoscale frontal dynamics in the North Pacific Subtropical Gyre. Geophys. Res. Lett. 43, 1651–1659. https://doi.org/10.1002/2015GL066996.

Long, Y., Zhu, X.-H., Guo, X., Huang, H., 2018. Temporal variation of Kuroshio nutrient stream south of Japan. J. Geophys. Res. Oceans 123. https://doi.org/10.1029/2017JC013635.

Luo, S., Jing, Z., Qi, Y., 2020. Submesoscale flows associated with convergent strain in an anticyclonic eddy of the Kuroshio Extension: A high-resolution numerical study. Ocean Sci. J. 55, 249–264. https://doi.org/10.1007/s12601-020-0022-x.

Mahadevan, A., 2016. The impact of submesoscale physics on primary productivity of plankton. Ann. Rev. Mar. Sci. 8, 161–184. https://doi.org/10.1146/annurev-marine-010814-015912.

McGillicuddy Jr., D.J., 2016. Mechanisms of physical-biological-biogeochemical interaction at the oceanic mesoscale. Ann. Rev. Mar. Sci. 8, 125–159. https://doi.org/10.1146/annurev-marine-010814-015606.

McWilliams, J.C., Gula, J., Molemaker, M.J., Renault, L., Shchepetkin, A.F., 2015. Filament frontogenesis by boundary layer turbulence. J. Phys. Oceanogr. 45, 1988–2005. https://doi.org/10.1175/JPO-D-14-0211.1.

McWilliams, J.C., 2016. Submesoscale currents in the ocean. Proc. Royal Soc. A 472, 20160117. https://doi.org/10.1098/rspa.2016.0117.

Nagai, T., Clayton, S., 2017. Nutrient interleaving below the mixed layer of the Kuroshio Extension Front. Ocean Dyn. 67, 1027–1046. https://doi.org/10.1007/s10236-017-1070-3.

Nagai, T., Clayton, S., Uchiyama, Y., 2019. Multiscale routes to supply nutrients through the Kuroshio nutrient stream. In: Nagai, T., Saito, H., Suzuki, K., Takahashi, M. (Eds.), Kuroshio current physical, biogeochemical, and ecosystem dynamics (Geophysical Monograph Series Book 243). AGU-Wiley, NJ, pp. 112–125.

Ning, J., Chen, K., Gaube, P., 2021. Diverse variability of surface chlorophyll during the evolution of Gulf Stream Rings. Geophys. Res. Lett. 48, e2020GL091461 https://doi.org/10.1029/2020GL091461.

Oka, E., Talley, L.D., Suga, T., 2007. Temporal variability of winter mixed layer in the mid-to high-latitude North Pacific. J. Oceanogr. 63, 293–307.

Omand, M.M., Mahadevan, A., 2013. Large-scale alignment of oceanic nitrate and density. J. Geophys. Res. 118, 5322–5332. https://doi.org/10.1002/jgrc.20379.

Pasqueron de Fommervault, O., D'Ortenzio, F., Mangin, A., Serra, R., Migon, C., Claustre, H., Lavigne, H., d'Alcala, M.R., Prieur, L., Taillandier, V., Schmechtig, C., Poteau, A., Leymarie, E., 2015. Seasonal variability of nutrient concentrations in the Mediterranean Sea: Contribution of Bio-Argo floats. J. Geophys. Res. 120, 8528–8550. https://doi.org/10.1002/2015jc011103.

Ren, H., Sigman, D.M., Martínez-García, A., Andersond, R.F., Chen, M.T., Ravelo, A.C., Straub, M., Wong, G.T.F., Haug, G.H., 2017. Impact of glacial/interglacial sea level change on the ocean nitrogen cycle. PNAS 114, E6759–E6766. https://doi.org/10.1073/pnas.1701315114.

Sakamoto, C.M., Johnson, K.S., Coletti, L.J., 2009. Improved algorithm for the computation of nitrate concentrations in seawater using an in situ ultraviolet spectrophotometer. Limnol. Oceanogr. Methods 7, 132–143. https://doi.org/10.4319/lom.2009.7.132.

Sakamoto, C.M., Johnson, K.S., Coletti, L.J., Jannasch, H.W., 2017. Pressure correction for the computation of nitrate concentrations in seawater using an in situ ultraviolet spectrophotometer. Limnol. Oceanogr. Methods 15, 897–902. https://doi.org/10.1002/lom3.10209.

Qiu, B., Chen, S., Schneiderd, N., 2017. Dynamical links between the decadal variability of the Oyashio and Kuroshio Extensions. J. Phys. Oceanogr. 30, 9591–9605. https://doi.org/10.1175/JCLI-D-17-0397.1.

Wang, T., Barkan, R., McWilliams, J.C., Molemaker, M.J., 2021. Structure of submesoscale fronts of the Mississippi River plume. J. Phys. Oceanogr., in press. https://doi.org/10.1175/JPO-D-20-0191.1.

While, J., Haines, K., 2010. A comparison of the variability of biological nutrients against depth and potential density. Biogeosciences 7, 1263–1269. https://doi.org/10.5194/bg-7-1263-2010.

Xing, X., Morel, A., Claustre, H., Antoine, D., D'Ortenzio, F., Poteau, A., Mignot, A., 2011. Combined processing and mutual interpretation of radiometry and fluorimetry from autonomous profiling Bio-Argo floats: Chlorophyll a retrieval. J. Geophys. Res. 116, C6. https://doi.org/10.1029/2010jc006899.

Xiu, P., Chai, F., 2020. Eddies affect subsurface phytoplankton and oxygen distributions in the North Pacific Subtropical Gyre. Geophys. Res. Lett. 47, e2020GL087037 https://doi.org/10.1029/2020gl087037.

Xu, L., Xie, S.-P., Jing, Z., Wu, L., Liu, Q., Li, P., Du, Y., 2017. Observing subsurface changes of two anticyclonic eddies passing over the Izu-Ogasawara Ridge: Changes of eddies passing over Izu Ridge. Geophys. Res. Lett. 44, 1857–1865. https://doi.org/10.1002/2016GL072163.

Xu, G., Dong, C., Liu, Y., Gaube, P., Yang, J., 2019. Chlorophyll rings around ocean eddies in the North Pacific. Sci. Rep. 9, 2056. https://doi.org/10.1038/s41598-018-38457-8.

Yang, Q., Zhao, W., Liang, X., Dong, J., Tian, J., 2017. Elevated mixing in the periphery of mesoscale eddies in the South China Sea. J. Phys. Oceanogr. 47, 895–907. https://doi.org/10.1175/JPO-D-16-0256.1.

Zhang, Z., Qiu, B., Klein, P., Travis, S., 2019. The influence of geostrophic strain on oceanic ageostrophic motion and surface chlorophyll. Nat. Commun. 10, 2838. https://doi.org/10.1038/s41467-019-10883-w.

Zhou, K., Dai, M., Kaoa, S., Wang, L., Xiu, P., Chai, F., Tian, J., Liua, Y., 2013. Apparent enhancement of 234Th-based particle export associated with anticyclonic eddies. Earth Planet. Sci. Lett. 381, 198–209. https://doi.org/10.1016/j.epsl.2013.07.039.